Nanonetworks of Multifunctional Polyhedral Oligomeric Silsesquioxane and Polypropylene Oxide

Yu Bian and Jovan Mijović*

Othmer-Jacobs Department of Chemical and Biological Engineering, Polytechnic Institute of New York University, Six Metrotech Center, Brooklyn, New York 11201

Received May 8, 2008; Revised Manuscript Received July 21, 2008

ABSTRACT: An investigation was carried out of the segmental and normal mode dynamics in multifunctional polyhedral oligomeric silsesquioxane (POSS)/polypropylene oxide (PPO) nanonetworks. The reaction kinetics and thermal properties of POSS/PPO nanonetworks are studied by Fourier transform infrared spectroscopy (FTIR), differential scanning calorimetry (DSC) and thermogravimetric analysis (TGA). Dynamic behavior is investigated by broadband dielectric relaxation spectroscopy (DRS) and dynamic mechanical spectroscopy (DMS) over a wide range of frequency and temperature. Before the onset of reaction, POSS nanoparticles promote motions of PPO chains in nanocomposites. During the formation of nanonetworks, however, the presence of POSS nanoparticles causes gradual increase in the time scale of the segmental (α) and the normal mode (α_N) process in POSS/PPO nanonetworks. Comparison of DRS and DMS results for the α process reveals identical trends with respect to POSS concentration and temperature. A detailed account of the effect of POSS structure, PPO molecular weight, extent of reaction and temperature on the molecular origin, temperature dependence and spectral characteristics of relaxation processes in POSS/PPO nanonetworks is provided. The results show how the properties of POSS/PPO nanonetworks can be controlled by the selection of POSS functional group and PPO molecular weight.

Introduction

Nanoscopic organic−inorganic hybrids are receiving considerable attention as reinforcement in composites due to their unique chemophysical properties, such as reduced flammability, increased oxidation resistance and improved mechanical properties.[1−3] Among various nanoreinforcements, polyhedral oligomeric silsesquioxane (POSS) is particularly interesting. POSS molecules consist of a rigid silica core with different organic moieties covalently bonded to the silicon atoms. A variety of organic groups can be attached to the silsesquioxane cage resulting in many possible structures, and hence properties of POSS/polymer nanocomposites. Generally, POSS can be incorporated into a polymer matrix either by (1) chemical tethering to the polymer chains (to pendant groups[4−11] or the polymer backbone[12−27]) or (2) physical blending.[28−40] Most commonly used polymer matrices are epoxy resins.

There are recent reports of studies of epoxy-functionalized POSS/amine systems and amine-functionalized POSS/epoxy systems. Examples include OctaGlycidyldimethylsilyl-POSS (OG)/diaminodiphenylmethane (DDM),[13,16,20,41,42] OctaEpoxyCyclohexyldimethylsilyl-POSS (OC)/DDM,[21,41,42] OctaAmminophenyl-POSS (OAPS)/diglycidyl ether of bisphenol A (DGEBA),[18,20] OAPS/pyromellitic dianhydride (PMDA)[15,17] and OG/meta-phenylenediamine (mPDA).[19] Those investigations report improved bulk thermomechanical properties of composites, such as thermal stability, glass transition temperature, char yield and storage modulus. However, there is a lack of information about the molecular motions that underlie physical and mechanical response of these systems, and that is where the knowledge of dynamics becomes important. By understanding molecular dynamics, we aim to tailor macroscopic behavior of these materials from nanoscopic concepts.

In this study, linear polypropylene oxide (PPO) with amine end groups was selected as matrix. PPO is a particularly informative host in the studies of chain dynamics in an applied electric field, because it contains type A dipoles[43−46] (first identified by Stockmayer and Baur) parallel to the polymer backbone, which relax by the motions of entire chains. This is in addition to the type B dipoles contributed by the transverse dipole moment component, which relax via segmental motions. The presence of type A dipoles also affords a direct comparison of dielectric and viscoelastic relaxation in these systems. Two multifunctional POSS monomers, each with different epoxy functionalized side group, were used to form POSS/PPO nanonetworks. The reaction kinetics, thermal properties and dynamics of the POSS/PPO nanonetworks were studied systematically by a host of experimental techniques.

The principal objective of this study is to elucidate the effect of the structure of POSS, molecular weight of PPO, extent of reaction and temperature on the dynamics of POSS/PPO nanonetworks.

Experimental Section

Materials. *Polymer.* Linear polypropylene oxide (PPO) with symmetrical dipole inversion was used as polymer matrix in this study. Two arms emanate from a central point, each containing an uninverted dipole sequence. Each arm is end-functionalized with a primary amine group as shown in Figure 1. Type A and B dipoles in this polymer give rise to the normal mode (α_N) process and the segmental (α) process, respectively. Two PPOs with molecular weights of 2 kg/mol (JEFFAMINE D-2000) and 4 kg/mol (JEFFAMINE D-4000) were obtained from Huntsman (www.huntsman.com).

Multifunctional POSS. Multifunctional POSS monomers possess a hybrid inorganic−organic three-dimensional structure and contain eight reactive organic functional groups as shown in Figure 2. The dimension of POSS cubic frame is around 1.2−1.5 nm. Two different multifunctional POSS monomers were selected for study: OctaGlycidyldimethylsilyl-POSS [OG] (EP0430), shown in Figure 2A, and OctaEpoxyCyclohexyldimethylsilyl-POSS [OC] (EP0435),

Figure 1. PPO architecture (amine functionalized linear PPO chain with symmetrically inverted dipoles).

* To whom correspondence should be addressed. E-mail: jmijovic@poly.edu.

10.1021/ma801044v CCC: $40.75
Published on Web 09/10/2008

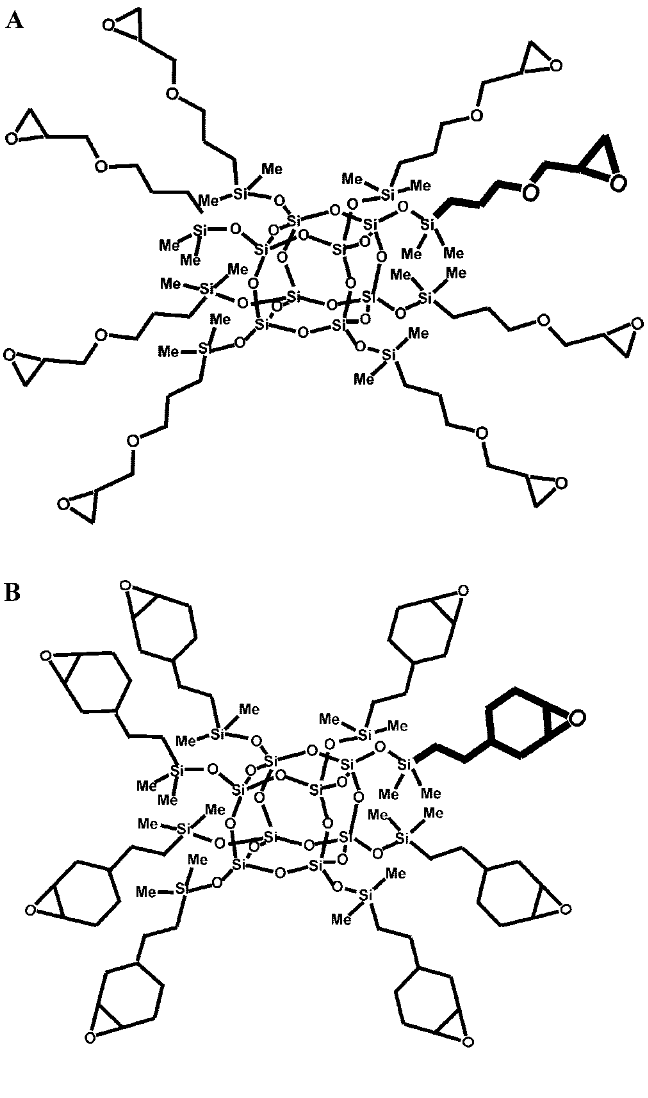

Figure 2. Chemical structure of multifunctional POSS monomers: (A) OctaGlycidyldimethylsilyl-POSS (OG); (B) OctaEpoxyCyclohexyldimethylsilyl-POSS (OC).

Table 1. OG/PPO and OC/PPO Nanocomposite Formulations Investigated

description	wt % of POSS in PPO	code
OG + PPO2	31.3	OGP2
OC + PPO2	20.1	OCP2
OG + PPO4	18.5	OGP4
OC + PPO4	11.2	OCP4

shown in Figure 2B. The side groups are different in OG and OC, although each contains a terminal epoxy group. Specifically they differ in that the end group epoxy ring is attached to a linear glycidyl moiety in OG and to a cyclohexyl ring in OC. At room temperature, OG is a liquid with a viscosity of 300 cP, while OC is a solid. The two POSS monomers were selected for study in order to elucidate the effect of side chain structure on network dynamics. POSS monomers were obtained from Hybrid Plastic (www.hybridplastics.com).

Reactive Mixture. A desired amount of POSS and PPO was mixed with toluene using a high-speed stirrer. Toluene evaporates fast, and good dispersions of POSS in PPO are obtained. The reaction is slow at room temperature. The mixtures were degassed prior to the measurement. The characteristics of the samples investigated are summarized in Table 1. In the sample code used throughout the paper, the first two letters define the type of POSS (OG or OC) and the last one, "P", stands for PPO with amine end groups. The number that follows defines the molecular weight of PPO in thousands. For example, OGP4 represents a nanocomposite of OctaGlycidyldimethylsilyl-POSS (OG) and amine-terminated PPO (P) with molecular weight of 4 kg/mol. The stoichiometric molar ratio of PPO and POSS is 2:1 in OGP nanocomposites and 4:1 in OCP nanocomposites.

Techniques. *Dielectric Relaxation Spectroscopy (DRS).* Our facility combines commercial and custom-made instruments that include (1) Novocontrol's α high-resolution dielectric analyzer (3 μHz to 10 MHz) and (2) Hewlett-Packard 4291B RF impedance analyzer (1 MHz to 1.8 GHz). Both instruments are interfaced to computers and equipped with heating/cooling controls, including the Novocool system custom-modified for measurements over the entire frequency range from 3 μHz to 1.8 GHz. The samples were placed between the stainless steel electrodes (we obtained identical results using aluminum electrodes). The diameter of the electrodes is 12 mm, and the sample thickness is 50 μm. Further details of our DRS facility are given elsewhere.[47−49]

Dynamic Mechanical Spectroscopy (DMS). Experiments were conducted using a Rheometric Scientific's Advanced Rheometric Expansion System (ARES) rheometer. Measurements were performed in the frequency range from 0.001 to 100 rad/s. Parallel plate configuration was employed with a typical gap between the plates of 0.5−1.5 mm. Strain values were adjusted from 0.2 to 25% for the measurable torque in the linear viscoelastic range.

Fourier Transform Infrared Spectroscopy (FTIR). FTIR spectroscopy was performed using a Nicolet Magna-IR system 750 spectrometer with spectral range coverage from 15,800 to 50 cm^{-1} and the Vectra interferometer with better than 0.1 cm^{-1} resolution. Near-infrared (NIR) data were obtained using a calcium fluoride beam splitter, a white light source and a mercury−cadmium−tellurium (MCT) detector. A silica type optical fiber was used for *in situ* monitoring of reactions in the remote mode. The details of our use of the technique may be found elsewhere.[49] The extent of reaction is calculated by comparing absorption of reactive groups at any given time during reaction to the initial absorption, and normalizing with respect to a group not involved in the reaction.

Differential Scanning Calorimetry (DSC). A TA Instrument Co. DSC model 2920 was used. The samples were placed in sealed DSC pans and scanned at a heating or cooling rate of 10 °C/min.

Thermogravimetric Analyzer (TGA). A TA Instrument Co. Hi-Res Modulated TGA model 2950 was used. Thermal stability of materials was tested under nitrogen. Samples (10−20 mg) were loaded in platinum pans and heated to 800 °C (20 °C/min N_2). The N_2 flow rate was 40 and 60 mL/min in the balance chamber and the furnace, respectively.

Results and Discussion

1. Kinetics of Nanonetwork Formation. We begin by describing the curing behavior of OGP and OCP. Chemical reactions between OG and OC with amine-terminated PPO lead to two different types of architecture depicted in Figure 3. In the course of formation of OGP nanonetworks, each amine hydrogen reacts with an epoxy group to form doubly bridging or bifurcated tethers as shown in Figure 3A. In OCP nanonetworks, however, only linear tethers form, as shown in Figure 3B. The steric hindrance introduced by the cyclohexyl ring in the OC side chain impedes the secondary amine−epoxy reaction. This phenomenon has also been reported by Laine,[21,41] and the spectroscopic evidence of it in our systems is provided below.

Curing of all nanocomposites was conducted at 120 °C, and the progress of reaction was monitored with near-infrared (NIR) spectroscopy by following the decrease in the absorption intensity of epoxy (~4500 cm^{-1}) and amine (~4940 cm^{-1}) peaks. An example of a series of NIR spectra generated during cure of OGP2 and OCP2 nanocomposites is presented in Figure 4. All characteristic absorption peaks for epoxy−amine systems are evident. The absorption intensities of reactive groups (epoxy and amine) decrease during reaction and vanish in fully cured nanonetworks. In the mid-IR spectra, we observe a pronounced peak at ~1100 cm^{-1} (not shown here) due to the symmetric

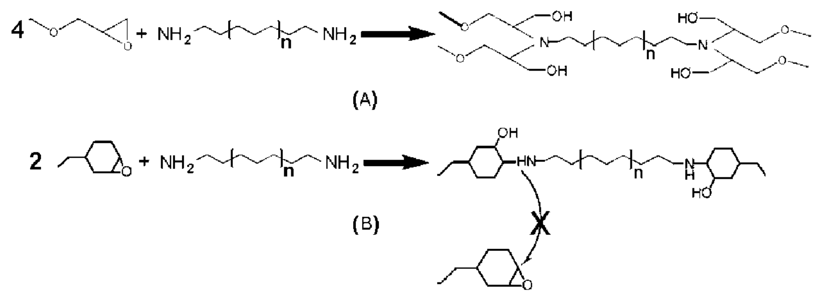

Figure 3. Reactions that lead to the formation of POSS/PPO nanonetworks, (a) OG/PPO and (b) OC/PPO.

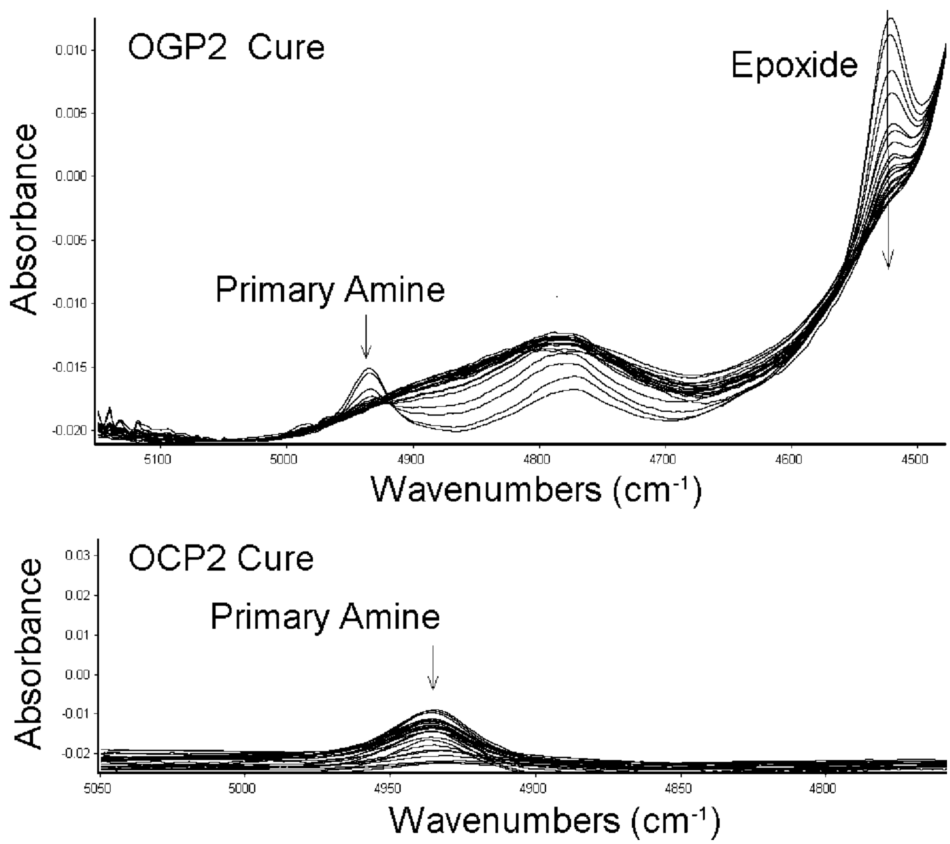

Figure 4. A series of NIR spectra obtained at various times during cure of OGP2 (above) and OCP2 (below) nanocomposites at 120 °C.

vibration of Si−O groups in the POSS cage. The presence of this peak[50,51] in all spectra indicates that the POSS cube structure remains unperturbed by the reaction; a degraded cube structure has been shown to result in a broader and asymmetric Si−O peak.[52−54] DSC and TGA data also show that OG and OC cages remain stable below 300 °C, which is well above the cure temperature of 120 °C.[20,21,41,42,49]

The extent of reaction is calculated from the initial peak areas of functional (reactive) and reference groups, $A_{f,0}$ and $A_{r,0}$, respectively, and their corresponding values at time t, $A_{f,t}$ and $A_{r,t}$, using the following equation:

$$a = 1 - (A_{f,t}A_{r,0})/(A_{f,0}A_{r,t}) \quad (1)$$

The functional group used in the calculation was epoxide in OGP nanocomposites and primary amine in OCP nanocomposites. The peak associated with the $-CH_3$ stretching absorption ~4320 cm^{-1} (not shown here) was used as a reference. The calculated extent of reaction for OGP and OCP nanocomposites with PPO molecular weight as a parameter is plotted as a function of reaction time in Figure 5, and several interesting observations are made. First, the reaction is faster in OGP nanocomposites because of the different molecular mechanism

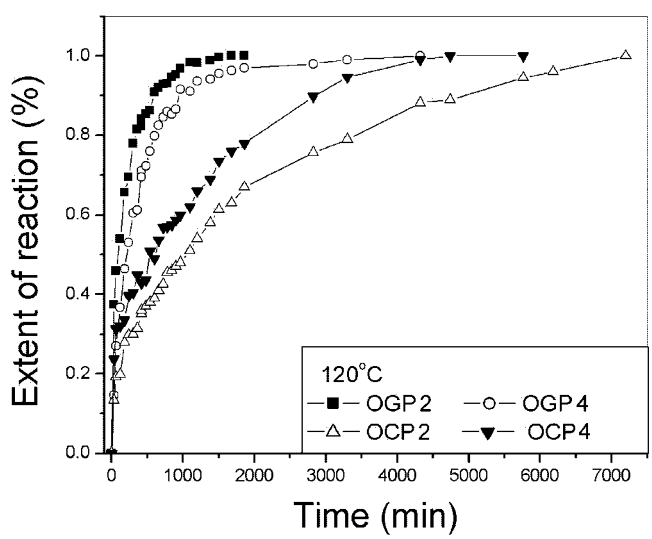

Figure 5. Extent of reaction as a function of time in four nanocomposites.

Table 2. Glass Transition Behavior and Thermal Stability for Neat OG, OC, PPO2, PPO4, Fully Cured OGP2, OGP4, OCP2 and OCP4 Nanocomposites

sample	T_g (°C)	T at 10 % wt loss (°C)	char yield	
			measd wt %	calcd wt %
OG	−78	383	38	
OC	−7	430	43	
PPO2	−70	315	0	
PPO4	−70	319	0	
OGP2	−55	353	13	12
OGP4	−64	331	7	7
OCP2	−60	356	10	9
OCP4	−66	353	5	5

and a higher solubility of OG in PPO. Second, the reaction rate is faster in OGP2 than OGP4 nanocomposites because of the higher weight fraction of OG in the former system. But in OCP nanocomposites the opposite is true because of a more pronounced OC aggregation that delays the reaction.

2. Thermal Properties. Characteristic thermal properties (glass transition temperature and the temperature for 10% weight loss and char yield) of all neat components (PPO2, PPO4, OG and OC) and fully cured nanonetworks (OGP and OCP) are listed in Table 2.

The glass transition temperature (T_g) of neat PPOs is not a function of molecular weight (DSC T_g = −70 °C). The calorimetric (DSC) T_g of OG is −78 °C. OC shows a weak glass transition at −7 °C and a melting point at 125 °C. OG is amorphous, and OC is crystalline. OC nanoparticles aggregate in the PPO matrix upon mixing during reaction, but the cured nanonetworks are transparent. A fully cured nanonetwork has a higher glass transition temperature than the corresponding neat PPO. In addition, a higher glass transition temperature was observed in OG than OC nanonetworks, because of the linear tether structure in the latter system. Finally, the PPO2 nanonetwork has a higher glass transition temperature than PPO4 since the network density increases with decreasing PPO chain length. The temperature difference between the T_g of OGP2 and OCP2 is larger (5 °C) than that between the T_g of OGP4 and OCP4 (2 °C).

The thermal behavior of neat OG, OC, PPO2 and PPO4 was also studied by TGA. The 10% mass loss is recorded at 315 °C for PPO2 and at 319 °C for PPO4. Neat PPOs undergo a complete mass loss at 400 °C.

The 10% mass loss temperature for OC is 430 °C, which is higher than OG by ∼50 °C. The char yield of OC (43%) in nitrogen (N_2) is higher than that of OG (38%), although OG has higher silica content. This is different from Choi,[21] who reports a higher char yield for OG. The presence of cyclohexyl groups in OC affords the additional thermal stability despite relatively low silica content. Fully cured nanonetworks with lower molecular weight PPO (PPO2) show a higher 10% mass loss temperature due to their more rigid structure. Compared with OGP with the same PPO molecular weight, OCP has a higher 10% mass loss temperature due to the more stable structure contributed by cyclohexyl groups. This is despite the fact that OCP nanonetworks have a linear tether structure.

Char yield is lower in OCP than OGP nanonetworks with the same PPO molecular weight because of the lower POSS concentration. A calculated char yield based on the rule of mixtures is included in Table 2. The measured and calculated values are similar, suggesting that the char yield depends only on the weight percentage of POSS and bears no relationship to the network architecture.

3. Dielectric Relaxation. *3.1. Neat PPO, OG and OC. 3.1.1. Neat PPO.* The background on the dielectric properties of polymers and other glass formers is nowadays available in many books and key reviews.[55−57] Dielectric response of neat

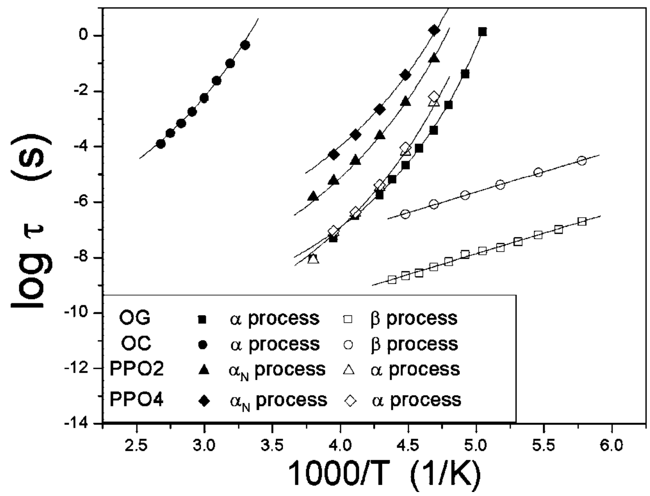

Figure 6. Temperature dependence of the average relaxation time for various relaxation processes in OG, OC, PPO2 and PPO4.

PPO has also been well documented in the literature,[43,45,46,48,49] and hence our goal here is not to be comprehensive. The experimentally obtained dielectric spectra in this study were deconvoluted using a sum of the well-known Havriliak−Negami (HN) functional[58] form and the conductivity term:

$$\varepsilon^*(\omega) = \varepsilon' - i\varepsilon'' = \sum_{k=1}^{n}\left[\varepsilon_{\infty k} + \frac{\varepsilon_{0k} - \varepsilon_{\infty k}}{(1 + (i\omega\tau_k)^{a_k})^{b_k}}\right] - i\left(\frac{\sigma}{\omega\varepsilon_v}\right)^N \quad (2)$$

where a_k and b_k are the shape parameters that define the breadth and the symmetry of the spectrum, respectively, σ is the conductivity, ε_v is the vacuum permittivity and τ_k is the average relaxation time obtained from the fits. The HN function reduces to the Debye equation when $a = b = 1$ and the Cole−Cole (CC) equation when $b = 1$.[59] The temperature dependence of the relaxation time for the segmental (τ_S) and normal (τ_N) mode processes confirms that the increase in molecular weight slows down the normal mode process but does not affect the segmental process. The temperature dependence of the average relaxation time for segmental and normal mode processes of neat PPO is of the Vogel−Fulcher−Tammann (VFT) type[55−57] described by

$$\tau = \tau_0 \exp\left(\frac{B}{T - T_v}\right) \quad (3)$$

Further details of our studies on the dynamics of neat PPO are available elsewhere.[48,49]

3.1.2. OG and OC. The DRS spectra of OG and OC (not shown here) reveal the following common features:[60] (1) both OG and OC undergo two relaxation processes, the α process due to the segmental motions of the side chains of POSS and the β process that originates from the local motions; (2) all processes shift to higher frequency with increasing temperature; and (3) dielectric strength decreases for the α process and increases for the β process with increasing temperature. But the differences between OG and OC dynamics are also notable. For example, the dielectric strength of the α process in OC is considerably smaller than in OG at a given temperature because of the lower concentration of mobile dipoles in the amorphous region of OC.

The temperature dependence of the average relaxation time for each process observed in OG, OC, PPO2 and PPO4 (obtained from the HN fits) was determined, and the results were plotted in Figure 6 (solid lines are fits). The temperature dependence of the average relaxation time follows the Vogel−Fulcher−Tammann (VFT) form for the α_N process in PPO and the α process in all

Table 3. VFT Parameters for Segmental and Normal Mode Relaxation in Neat PPO2, PPO4, OG and OC

	normal mode			segmental mode		
material	τ_0 (s)	B (k)	T_v (K)	τ_0 (s)	B (k)	T_v (K)
PPO2	4.5×10^{-13}	1534	154	1.0×10^{-14}	1559	154
PPO4	1.1×10^{-11}	1414	155	1.0×10^{-14}	1519	155
OG				5.7×10^{-13}	1114	159
OC				5.6×10^{-10}	2209	197

compounds. The Arrhenius form describes the β process in OG and OC. The corresponding VFT parameters are listed in Table 3. The longer time scale of the segmental process in OC is due to the higher T_g. The β process is slower in OC than OG because of the increased rigidity of side chains in the former molecule due to the incorporation of the cyclohexyl ring. The β process has similar activation energy in both compounds (ca. 29 kJ/mol), suggesting a common molecular origin.

3.2. Nanonetwork Dynamics during Cure. The effect of cure on the dynamics of four nanonetworks (OGP2, OGP4, OCP2 and OCP4) is discussed next. As previously stated, the extent of reaction in each network was determined from the kinetic data.

The dielectric permittivity (inset) and dielectric loss in the frequency domain with extent of reaction as a parameter for OGP2 and OGP4 are shown in Figures 7A and 7B, respectively. We observe a systematic decrease during cure in the limiting low frequency permittivity (ε'_0) and the maximum loss value (ε''_{max}), as well as the concomitant increase in the time scale (shift to lower frequency) of both segmental and normal mode relaxation processes. Dielectric loss in the frequency domain with extent of reaction as a parameter for OCP2 and OCP4 is shown in Figures 8A and 8B, respectively. Here, too, the average relaxation time for segmental and normal mode relaxation increases with increasing extent of reaction. Interestingly, however, the maximum loss value (ε''_{max}) for the segmental process in OCP nanonetworks initially increases with increasing extent of the reaction, reaches a maximum and then decreases.

We shall elaborate on this observation later. In all nanonetworks, at any given extent of reaction, the segmental and normal mode processes show the usual temperature dependence on frequency.

The best fits of the loss spectra were obtained using the HN functional form for the segmental process and the CC functional form for the normal mode process. The most pronounced changes in the dielectric spectra in going from unreacted mixtures to fully cured nanonetworks can be summarized as follows: (1) the normal mode process remains active at all stages of cure, including the fully cured nanonetwork, despite a notable change in the spectral shape; (2) the spectra of the unreacted mixture are thermodielectricically simple but turn complex shortly after the onset of reaction; (3) the dielectric strength of segmental and normal mode relaxation in the fully cured nanonetworks increases with decreasing temperature, but not nearly as much as in the unreacted mixture.

In what follows, we shall build a more detailed discussion of the nanonetwork dynamics around the effect of temperature and extent of reaction on three principal dynamic parameters: (1) the average relaxation time; (2) the shape of the relaxation spectra; and (3) the dielectric relaxation strength.

3.2.1. Average Relaxation Time. The temperature dependence of the average relaxation time for segmental and normal mode processes retains the VFT functional form throughout cure. The best-fit VFT parameters for all four nanonetworks are summarized in Tables 4 and 5. We stress that τ_0 for the segmental process in all systems was set at the attempt frequency (10^{-14} s) and the same Vogel temperature was used to fit the segmental and the normal mode process.[49] In Figure 9 we plot the average relaxation time for the segmental process (τ_S, Figure 9A) and the normal mode

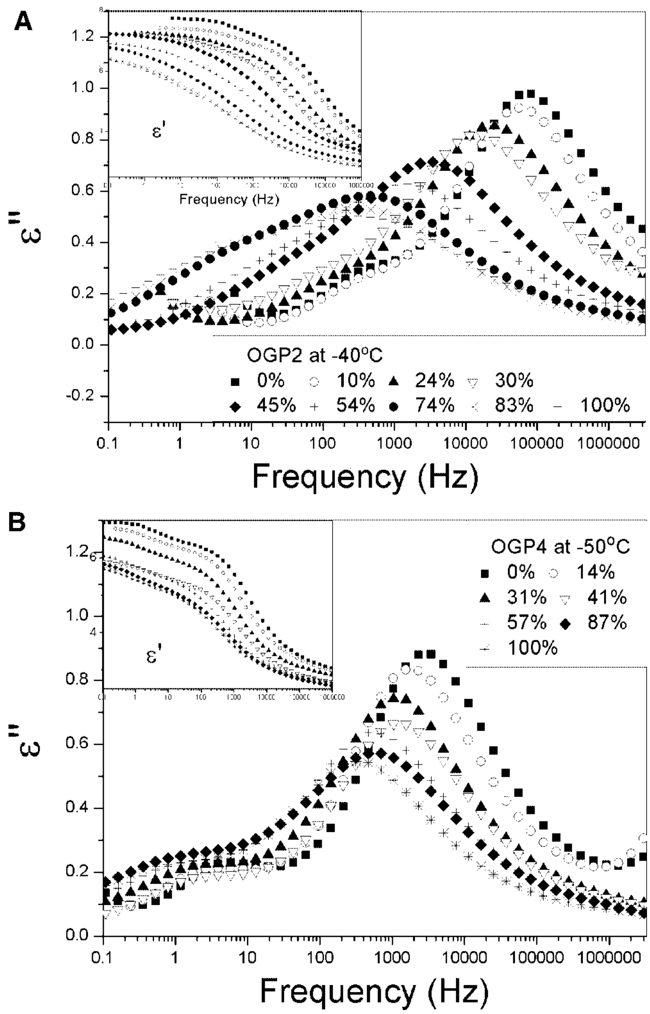

Figure 7. (A) Dielectric loss and permittivity (inset) for OGP2 nanocomposite at −40 °C in the frequency domain with extent of reaction as a parameter. (B) Dielectric loss and permittivity (inset) for OGP4 nanocomposite at −50 °C in the frequency domain with extent of reaction as a parameter.

process (τ_N, Figure 9B) in four nanonetworks (OGP2, OGP4, OCP2 and OCP4) at −50 °C with extent of reaction as a parameter. Since the experimental error is similar in all systems, only data for OGP2 are plotted with error bars in Figures 9 and 11. The data for the neat PPO2 and PPO4 are included for completion. The relaxation time for both segmental and normal mode process increases with increasing extent of reaction in all nanocomposites, and the discussion below will begin by contrasting the results observed at the extremes of 0% and 100% extent of reaction. The intent is to accentuate the effect of PPO molecular weight and POSS type on the network dynamics.

The average relaxation time of the segmental and normal mode process for the nanocomposites at the beginning of the reaction is examined first. Incorporation of POSS into the PPO matrix triggers two opposing effects on the nanocomposite dynamics: (1) the hindering effect due to the formation of covalent bonds between PPO and POSS and (2) the promoting effect due to the unreacted POSS nanoparticles which act as hard sphere diluents in the polymer matrix, decreasing the polymer self-association interactions and thus speeding up the motions of polymer chains. The promoting effect was observed in nonreactive POSS/PPO nanocomposites and was discussed in recent papers.[60,61] Figures 9A and 9B reveal that all unreacted nanocomposites exhibit longer τ_N and τ_S than the corresponding neat PPOs, indicating that the hindering effect is stronger than the promoting effect in the early stage of cure. We define $\boldsymbol{\Delta\tau}$ as the difference between the relaxation time of

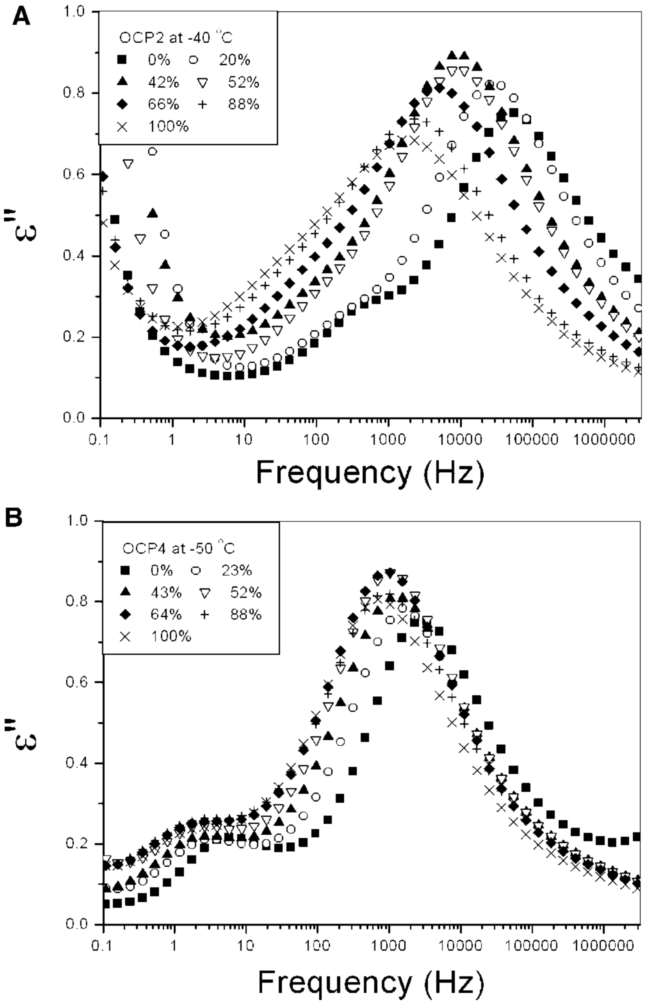

Figure 8. (A) Dielectric loss for OCP2 nanocomposite at −40 °C in the frequency domain with extent of reaction as a parameter. (B) Dielectric loss for OCP4 nanocomposite at −50 °C in the frequency domain with extent of reaction as a parameter.

Table 4. VFT Parameters for Segmental and Normal Mode Relaxation in OGP2 and OGP4 Nanocomposites during Reaction

extent of reaction	normal mode			segmental mode		
	τ_0 (s)	B (k)	T_v (K)	τ_0 (s)	B (k)	T_v (K)
OGP2: 0%	8.4×10^{-12}	1395	155	1.0×10^{-14}	1562	155
OGP2: 10%	2.8×10^{-10}	1027	156	1.0×10^{-14}	1573	156
OGP2: 24%	1.0×10^{-10}	1210	158	1.0×10^{-14}	1596	158
OGP2: 45%	3.8×10^{-11}	1327	162	1.0×10^{-14}	1609	162
OGP2: 54%	1.5×10^{-11}	1348	164	1.0×10^{-14}	1615	164
OGP2: 83%	1.4×10^{-11}	1370	165	1.0×10^{-14}	1635	165
OGP2: 100%	5.1×10^{-12}	1393	167	1.0×10^{-14}	1670	167
OGP4: 0%	1.4×10^{-11}	1386	159	1.0×10^{-14}	1523	159
OGP4: 14%	1.0×10^{-10}	1253	160	1.0×10^{-14}	1519	160
OGP4: 31%	2.8×10^{-10}	1196	161	1.0×10^{-14}	1504	161
OGP4: 41%	1.0×10^{-10}	1258	162	1.0×10^{-14}	1451	162
OGP4: 57%	5.6×10^{-11}	1322	163	1.0×10^{-14}	1480	163
OGP4: 87%	2.3×10^{-11}	1374	164	1.0×10^{-14}	1504	164
OGP4: 100%	1.4×10^{-11}	1386	164	1.0×10^{-14}	1513	164

a nanonetwork and the corresponding PPO (subscripts S and N represent the segmental and normal processes respectively) and observe the following order:

$$\Delta\tau_{S-OCP2} > \Delta\tau_{S-OGP4} > \Delta\tau_{S-OCP4} > \Delta\tau_{S-OGP2}$$
$$\Delta\tau_{N-OGP2} > \Delta\tau_{N-OGP4} > \Delta\tau_{N-OCP4} > \Delta\tau_{N-OCP2}$$

In fully cured nanonetworks, however, we observe a different response, in that the promoting effect is negligible in comparison

Table 5. VFT Parameters for Segmental and Normal Mode Relaxation in OGP2 and OGP4 Nanocomposites during Reaction

extent of reaction	normal mode			segmental mode		
	τ_0 (s)	B (k)	T_v (K)	τ_0 (s)	B (k)	T_v (K)
OCP2: 0%	1.0×10^{-10}	1320	156	1.0×10^{-14}	1572	156
OCP2: 20%	9.2×10^{-11}	1180	158	1.0×10^{-14}	1582	158
OCP2: 42%	1.9×10^{-11}	1257	159	1.0×10^{-14}	1616	159
OCP2: 52%	7.6×10^{-12}	1380	159	1.0×10^{-14}	1628	159
OCP2: 66%	1.5×10^{-12}	1475	160	1.0×10^{-14}	1661	160
OCP2: 88%	3.8×10^{-13}	1568	161	1.0×10^{-14}	1676	161
OCP2: 100%	3.4×10^{-14}	1886	161	1.0×10^{-14}	1710	161
OCP4: 0%	1.4×10^{-11}	1296	157	1.0×10^{-14}	1505	157
OCP4: 23%	2.3×10^{-11}	1421	161	1.0×10^{-14}	1457	161
OCP4: 43%	6.2×10^{-11}	1487	162	1.0×10^{-14}	1460	162
OCP4: 52%	3.8×10^{-11}	1571	163	1.0×10^{-14}	1468	163
OCP4: 64%	2.1×10^{-11}	1580	163	1.0×10^{-14}	1481	163
OCP4: 88%	1.4×10^{-11}	1609	163	1.0×10^{-14}	1456	163
OCP4: 100%	5.1×10^{-12}	1675	164	1.0×10^{-14}	1459	164

with the hindering effect. It is also clear that τ_S and τ_N in fully cured OGP2 (or OCP2) nanonetwork are longer than in OGP4 (or OCP4) due to the more rigid network architecture with lower molecular weight PPO. The fully cured OCP nanonetworks have shorter τ_S and τ_N than OGP.

3.2.2. Relaxation Spectra. The changes in the relaxation spectra during reaction are also revealing. The spectral breadth,

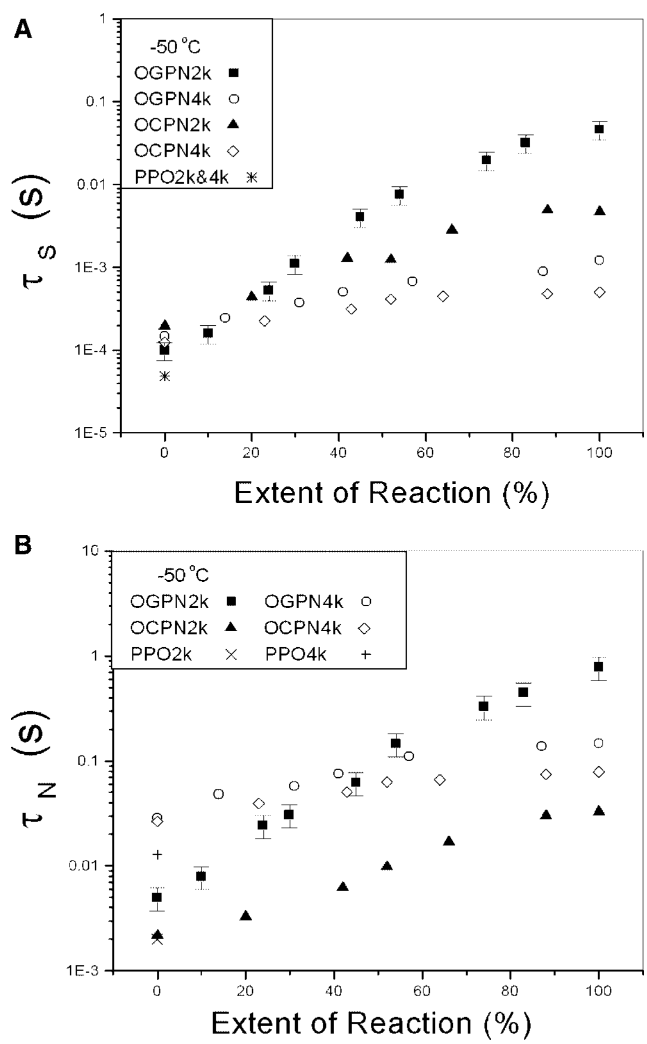

Figure 9. (A) Average relaxation time of the segmental process in four nanocomposites as a function of extent of reaction at −50 °C. (B) Average relaxation time of the normal mode process in four nanocomposites as a function of extent of reaction at −50 °C.

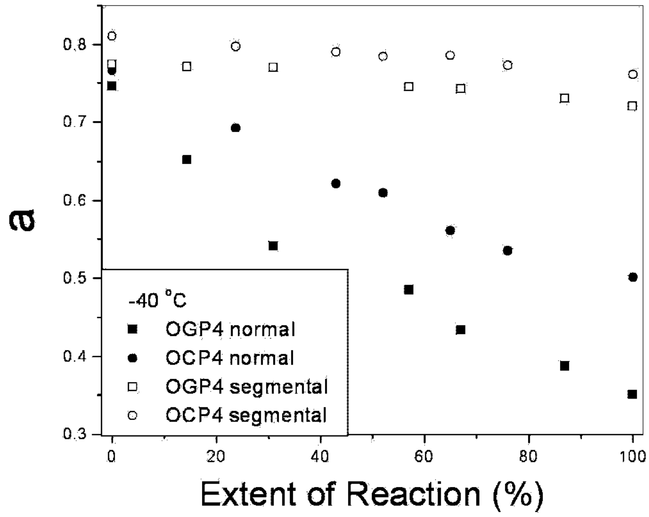

Figure 10. The HN parameter **a** for segmental and normal mode processes in OGP4 and OCP4 nanonetworks as a function of extent of reaction at −40 °C.

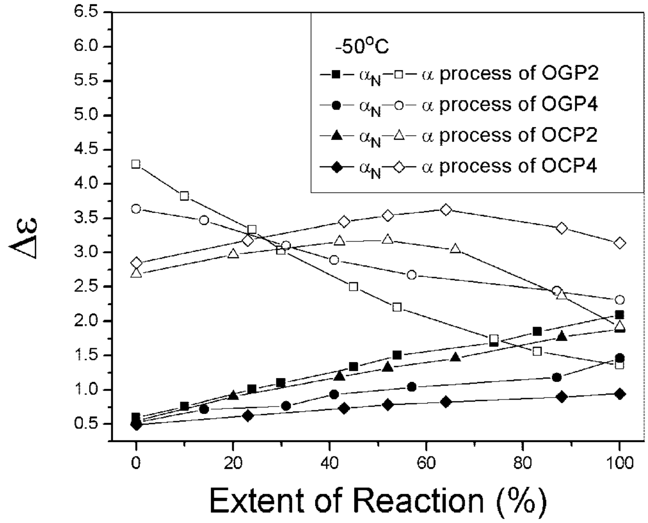

Figure 11. Dielectric relaxation strength for segmental and normal mode relaxation in four nanonetworks (OGP2, OGP4, OCP2 and OCP4) as a function of extent of reaction measured at −50 °C.

described by the HN parameter **a** is discussed first. Figure 10 illustrates the change in this parameter during reaction in OGP4 and OCP4 nanonetworks. A steady decrease in **a** during reaction is the signature of spectral broadening.[62−64] We define Δa as the difference in the parameter **a** between the initial mixture and the fully cured nanonetworks. Subscripts S and N represent the segmental and the normal process, respectively. For example: Δa_S and Δa_N at −40 °C are 0.10 and 0.41 for OGP2, 0.05 and 0.39 for OGP4, 0.08 and 0.37 for OCP2 and 0.04 and 0.26 for OCP4, respectively. The principal findings are summarized as follows: (1) Δa_S is smaller than Δa_N in all nanonetworks, because the global motion of PPO chains is more sensitive to the network formation than segmental relaxation; (2) OGP2 (or OCP2) nanonetworks have a greater Δa than OGP4 (or OCP4); and (3) OGP nanonetworks have greater Δa than OCP with PPO of the same molecular weight.

The HN parameter **b**, which defines the spectral symmetry, does not change with the extent of reaction for either segmental or normal mode process at a given temperature. For example: for segmental process at −40 °C, $b_{OGP2} = 0.30$, $b_{OGP4} = 0.50$, $b_{OCP2} = 0.40$ and $b_{OCP4} = 0.55$.

The segmental and normal mode spectra become thermodielectrically complex (the unreacted mixtures are simple) shortly after the onset of reaction and remain such until the completion of cure. For the segmental process, parameters **a** and **b** increase with increasing temperature; for the normal mode process, parameter **a** increases with increasing temperature, but **b** remains equal to 1.

3.2.3. Relaxation Strength. The effect of extent of reaction on the dielectric strength of OGP and OCP nanonetworks is described next. The relaxation strength ($\Delta\varepsilon$) is an important materials characteristic that depends on the chemical structure and molecular architecture. Relaxation strength of a given process is defined as $\Delta\varepsilon = \varepsilon'_0 - \varepsilon'_\infty$, where ε'_0 and ε'_∞ represent the limiting low- and high-frequency dielectric permittivity, respectively, for a particular mode (segmental or normal), and is proportional to the concentration of dipoles and the mean-squared dipole moment per molecule. The dielectric relaxation strength for the segmental mode ($\Delta\varepsilon_S$) and the normal mode ($\Delta\varepsilon_N$) at −50 °C were calculated from the fits of data and are shown in Figure 11. In the course of cure we observe a decrease in $\Delta\varepsilon_S$ of about 68% in OGP2 and 37% in OGP4. The $\Delta\varepsilon_S$ of OCP nanonetworks has a maximum value at 50% cure for OCP2 and at 65% for OCP4. The increase in $\Delta\varepsilon_N$ is about 250% in OGP2, 175% in OGP4, 210% in OCP2 and 92% in OCP4.

The dielectric relaxation strength for the segmental mode ($\Delta\varepsilon_S$) is discussed first. For OGP nanonetworks, the observed decrease in the limiting low-frequency dielectric permittivity (ε_0') with increasing extent of reaction, which drives the decrease in $\Delta\varepsilon_S$, is a direct consequence of the changing nature of the segmental process, reflecting a diminishing ability of dipolar moieties to store the electric field. Specifically, the decrease in $\Delta\varepsilon_S$ with increasing extent of reaction is attributed to the changes in the physical architecture (topology) of the network caused by the reactions and the change in the chemical nature of the dipole unit (epoxy and primary amine groups are replaced by the lesser dipole strength tertiary amine and hydroxyl groups, the latter being at the origin of the localized β process). Whereas $\Delta\varepsilon_S$ of OGP nanonetworks decreases monotonically during cure due to network formation, $\Delta\varepsilon_S$ of OCP nanonetworks exhibits a maximum due to the opposing effects of the disappearance of OC crystals and the growth of the network. Due to the presence of crystals, the segmental process in OC has a lower dielectric strength and a longer time scale than in OG. The reaction of OC with PPO is accompanied by the transformation of crystals into amorphous state. This leads to a decrease in the time scale of the segmental process in OC, a partial overlap with the segmental process of PPO and a concomitant increase in $\Delta\varepsilon_S$ of OCP nanonetworks. However, with further growth of the OCP network, the ability of dipolar moieties to store electric field decreases and so does the $\Delta\varepsilon_S$ of OCP nanonetworks.

As seen in Figure 11, the increase in $\Delta\varepsilon_N$ shows the following trend: $\Delta\varepsilon_{N\text{-}OGP2} > \Delta\varepsilon_{N\text{-}OCP2} > \Delta\varepsilon_{N\text{-}OGP4} > \Delta\varepsilon_{N\text{-}OCP4}$. This observation is similar to the previously reported result for DGEBA/PPO composites,[49] though the underlying physics remains incompletely understood.

4. Dynamic Mechanical Properties. The results of dynamic mechanical spectroscopy (DMS) during reaction are described next. We present only the data for OGP4 and OCP4 nanocomposites because analogous results were observed for OGP2 and OCP2. Storage and loss (inset) modulus in the frequency domain for OGP4 and OCP4 nanonetworks at −50 °C with extent of reaction as a parameter are shown in Figures 12 and 13, respectively. Data were shifted with respect to the reference curve at −50 °C. It is apparent that the variation in extent of reaction affects the viscoelastic response of OGP4 and OCP4 nanocomposites in segmental and terminal zones. In the terminal relaxation zone, the slopes of G' and G'' vs ω are 2 and 1, respectively, before the onset of reaction and then decrease during cure. Upon

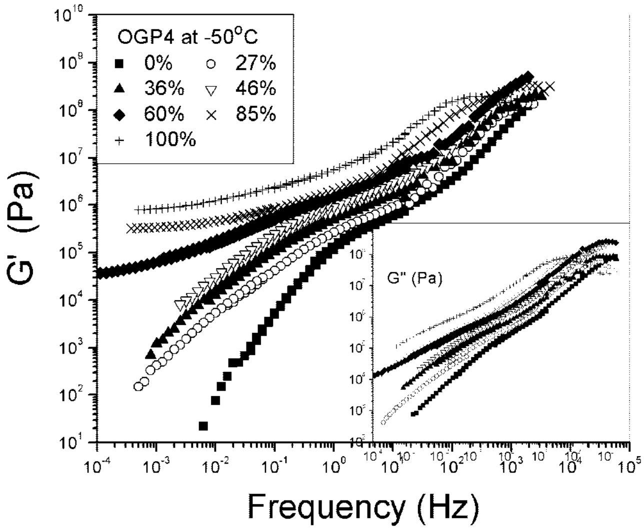

Figure 12. Storage modulus and loss modulus (inset) in the frequency domain with extent of reaction as a parameter for OGP4 nanocomposite at −50 °C. The curves were shifted horizontally using data at −50 °C as a reference.

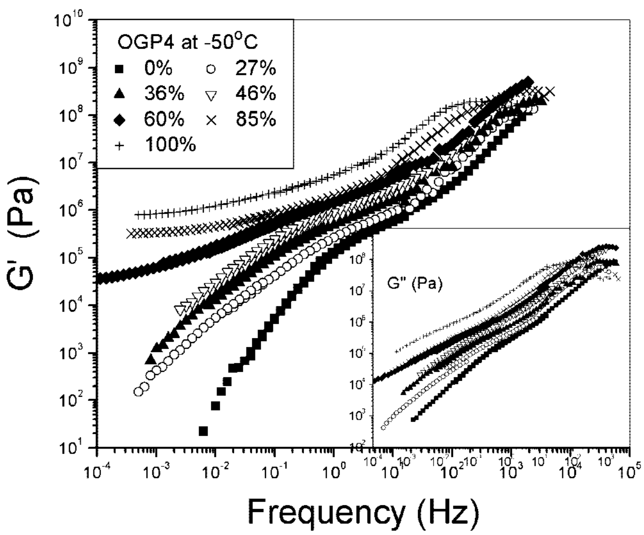

Figure 13. Storage modulus and loss modulus (inset) in the frequency domain with extent of reaction as a parameter for OCP4 nanocomposite at −50 °C. The curves were shifted horizontally using data at −50 °C as a reference.

completion of cure, the slopes of G' and G'' vs ω are 0.1 and 0.6 for OGP4 nanonetworks and 1.13 and 0.95 for OCP4 nanonetworks. The G' plateau in the terminal relaxation zone of OGP4 at the end of cure is a signature of solid-like behavior, while OCP4 remains still liquid-like. The operational gel point,[65] identified by the overlapping straight lines of G' and G'' with the same slope of 0.75, was recorded at 55% conversion for OGP4. The classic Flory formula[66] for conversion at gel point yields a value of about 50%, close to our result. However, OCP4 nanocomposite apparently retains liquid-like characteristics throughout cure, as no gel point is detected.

Finally, we focus attention on a comparative analysis of DRS and DMS results. Figure 14 shows the average relaxation time of the segmental mode in OGP4 and OCP4 nanonetworks as a function of extent of reaction measured at −60 °C and obtained from DRS (filled symbols) and DMS (open symbols) results. The average relaxation time from both DRS and DMS data was determined from $\tau_S = 1/\omega_{max} = 1/(2\pi f_{max})$. From Figure 14, we notice that the time scale of OCP4 dielectric relaxation is

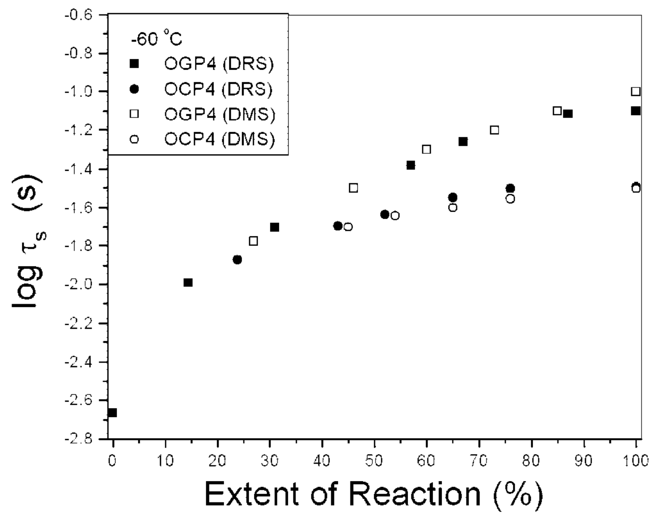

Figure 14. A comparison of DRS and DMS average relaxation time for the segmental process measured at −60 °C in OGP4 nanocomposite and OCP4 nanocomposite as a function of the extent of cure reaction.

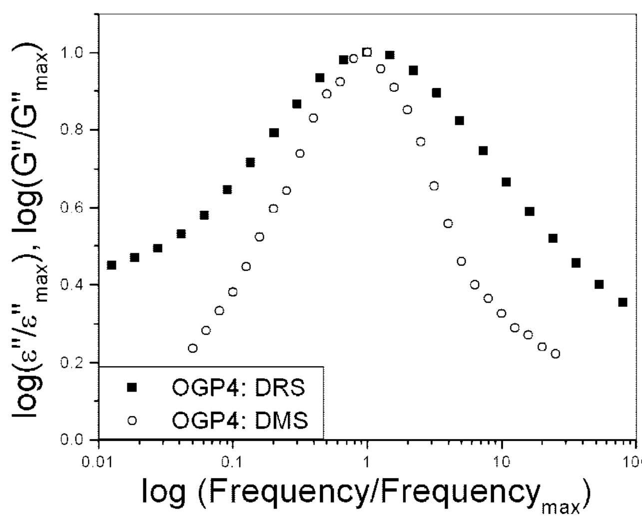

Figure 15. A comparison of normalized DRS and DMS spectra for the segmental process in fully cured OGP4 nanonetwork.

longer compared with DMS results because it is in liquid state in whole stage of the reaction. It is same as the Buchenau's[67] observations in highly viscous glass formers. The long dielectric relaxation time is attributed to the influence of the viscosity. However, OGP4 follows the opposite trends because of the solid network formation, and the different mechanism should be proposed. The normal mode relaxation was not compared because of the difficulties in deconvoluting the normal mode process from the DMS spectra with increasing extent of reaction.

A comparison of the normalized DRS and DMS spectra for the segmental process in fully cured OGP4 nanonetwork is illustrated in Figure 15. Clearly, the DRS spectra are broader. The same phenomenon was observed in the nonreactive POSS/PPO nanocomposites[60] and other epoxy/amine networks.[48]

Conclusions

We have completed an investigation of the dynamics of multifunctional POSS/PPO nanonetworks. The effect of POSS type and PPO molecular weight on the properties of POSS/PPO nanonetworks at various stages of cure was elucidated, and our principal conclusions are summarized below.

The architecture of POSS side groups plays an important role in the topology of nanonetworks. A doubly bridging tether forms in OGP nanonetworks, while a linear tether forms in OCP nanonetworks due to the steric hindrance introduced by the cyclohexyl ring in the side chain.

The unreacted POSS nanoparticles in the PPO matrix speed up the motion of polymer chains by decreasing the self-association interactions. But the formation of covalent bonds between POSS and PPO has the opposite effect on dynamics as it increases the time scale of relaxation. This interplay between the promoting and the hindering effect on dynamics varies during cross-linking. The segmental and the normal mode process in nanonetworks become slower and broader in the course of the reaction. The dielectric strength of the segmental process in OCP nanonetworks exhibits a maximum due to the opposing effects of the disappearance of OC crystals and the formation of cross-links. In OGP nanonetworks, however, the dielectric strength decreases continuously during cross-linking.

The properties of the fully cured POSS/PPO nanonetworks are controlled by the network structure. The higher cross-link density imparted by the double bridging tether in OGP nanonetworks results in a higher T_g, slower segmental and normal mode relaxation and broader spectra. PPO with lower molecular weight forms more rigid networks, and that results in higher T_g and 10% mass loss temperature, slower segmental and normal mode relaxation and broader spectra.

The operational gel point is recorded at 55% conversion for OGP4. No gel point is detected for OCP4 nanonetworks as these display liquid-like characteristics at all stages of cure. A flat G' in the terminal relaxation zone of fully cured OGP nanonetworks is a signature of solid-like behavior. The time scale of the segmental relaxation in OCP4 nanonetworks is longer in DRS than DMS spectra, but the opposite is true for OGP4 nanonetworks. A comparison of the normalized DRS and DMS spectra for the segmental process shows that the former are broader.

Acknowledgment. This work is supported by National Science Foundation under Grant DMR-0346435.

References and Notes

(1) Whitesides, G. M.; Mathias, T. P.; Seto, C. T. *Science* **1991**, *254*, 1312.
(2) Krishnamoorti, R.; Vaia, R. A. *Polymer Nanocomposites—Synthesis, Characterization and Modeling*; ACS Symposium Series; ACS: Washington, DC, 2001; Vol. *804*.
(3) Nalwa, H. S. *Handbook of Organic-Inorganic Hybrid Materials and Nanocomposites, Vol. 2, Nanocomposites*; American Scientific Publishers: Stevenson Ranch, CA, 2003.
(4) Zheng, L.; Hong, S.; Cardoen, G.; Burgaz, E.; Gido, S. P.; Coughlin, E. B. *Macromolecules* **2004**, *37*, 8606.
(5) Turri, S.; Levi, M. *Macromolecules* **2005**, *38*, 5569.
(6) Liu, H.; Zheng, S.; Nie, K. *Macromolecules* **2005**, *38*, 5088.
(7) Huang, C.; Kuo, S.; Lin, F.; Huang, W.; Wang, C.; Chen, W.; Chang, F. *Macromolecules* **2006**, *39*, 300.
(8) Drazkowski, D. B.; Lee, A.; Haddad, T. S.; Cookson, D. J. *Macromolecules* **2006**, *39*, 1854.
(9) Bizet, S.; Galy, J.; Gerard, J. *Macromolecules* **2006**, *39*, 2574.
(10) Tsuchida, A.; Bolln, C.; Sernetz, F. G.; Frey, H.; Mulhaupt, R. *Macromolecules* **1997**, *30*, 2818.
(11) Romo-Uribe, A.; Mather, P. T.; Haddad, T. S.; Lichtenhan, J. D. *J. Polym. Sci., Part B: Polym. Phys.* **1998**, *36*, 1857.
(12) Li, G.; Wang, L. C.; Toghiani, H.; Daulton, T. L.; Koyama, K.; Pittman, C. U. *Macromolecules* **2001**, *34*, 8686.
(13) Choi, J.; Harcup, J.; Yee, A. F.; Zhu, Q.; Laine, R. M. *J. Am. Chem. Soc.* **2001**, *123*, 11420.
(14) Li, G.; Thompson, T.; Daulton, T. L.; Pittman, C. U. *Polymer* **2002**, *43*, 4167.
(15) Choi, J.; Tamaki, R.; Kim, S. G.; Laine, R. M. *Chem. Mater.* **2003**, *15*, 3365.
(16) Kim, G. M.; Qin, H.; Fang, X.; Sun, F. C.; Mather, P. T. *J. Polym. Sci., Part B: Polym. Phys.* **2003**, *41*, 3299.
(17) Tamaki, R.; Choi, J.; Laine, R. M. *Chem. Mater.* **2003**, *15*, 793.
(18) Ni, Y.; Zheng, S.; Nie, K. *Polymer* **2004**, *45*, 5557.
(19) Chen, W.; Wang, Y.; Kuo, S.; Huang, C.; Tung, P.; Chang, F. *Polymer* **2004**, *45*, 6897.
(20) Choi, J.; Kim, S. G.; Laine, R. M. *Macromolecules* **2004**, *37*, 99.
(21) Choi, J.; Yee, A. F.; Laine, R. M. *Macromolecules* **2004**, *37*, 3267.
(22) Liang, K.; Toghiani, H.; Li, G.; Pittman, C. U. *J. Polym. Sci., Part A: Polym. Chem.* **2005**, *43*, 3887.
(23) Li, G. Z.; Cho, H.; Wang, L.; Toghiani, H.; Pittman, C. U., Jr. *J. Polym. Sci., Part A: Polym. Chem.* **2005**, *43*, 355.
(24) Cho, H.; Liang, K.; Chatterjee, S.; Pittman, C. U. *J. Inorg. Organomet. Polym. Mater.* **2005**, *15*, 541.
(25) Liang, K.; Li, G.; Toghiani, H.; Koo, J. H.; Pittman, C. U. *Chem. Mater.* **2006**, *18*, 301.
(26) Patel, R. R.; Mohanraj, R.; Pittman, C. U. *J. Polym. Sci., Part B: Polym. Phys.* **2006**, *44*, 234.
(27) Zhang, Y.; Lee, S.; Yoonessi, M.; Liang, K.; Pittman, C. U. *Polymer* **2006**, *47*, 2984.
(28) Lichtenhan, J. D. *Comments Inorg. Chem.* **1995**, *17*, 115.
(29) Lichtenhan, J. D.; Noel, C. J.; Bolf, A. G.; Ruth, P. N. *Mater. Res. Soc. Symp. Proc.* **1996**, *435*, 3.
(30) Haddad, T. S.; Lichtenhan, J. D. *Macromolecules* **1996**, *29*, 7302.
(31) Schwab, J. J.; Haddad, T. S.; Lichtenhan, J. D.; Mather, P. T.; Chaffee, K. P. *Annu. Tech. Conf. Soc. Plastics Eng.* **1997**, *611*, 1817.
(32) Mather, P. T.; Jeon, H. G.; RomoUribe, A.; Haddad, T. S.; Lichtenhan, J. D. *Macromolecules* **1998**, *32*, 1194.
(33) Fu, B. X.; Hsiao, B. S.; Pagola, S.; Stephens, P.; White, H.; Rafailovich, M.; Mather, P. t.; Jeon, H. G.; Phillips, S.; Lichtenhan, J. D.; Schwab, J. J. *Polymer* **2000**, *45*, 599.
(34) Zheng, L.; Farris, R. J.; Coughlin, E. B. *Macromolecules* **2001**, *34*, 8034.
(35) Xu, H. Y.; Kuo, S. W.; Lee, J. S.; Chang, F. C. *Macromolecules* **2002**, *35*, 8788.
(36) Xu, H. Y.; Kuo, S. W.; C., C. F. *Polym. Bull. (Berlin)* **2002**, *34*, 469.
(37) Fu, B. X.; Gelfer, M. Y.; Hsiao, B. S.; Phillips, S.; Viers, B.; Blanski, R.; Ruth, P. *Polymer* **2003**, *44*, 1499.
(38) Kopesky, E. T.; Haddad, T. S.; Cohen, R. E.; McKinley, G. H. *Macromolecules* **2004**, *37*, 8992.
(39) Capaldi, F. M.; Rutledge, G. C.; Boyce, M. C. *Macromolecules* **2005**, *38*, 6700.
(40) Joshi, M.; Butola, B. S.; Simon, G.; Kukaleva, N. *Macromolecules* **2006**, *39*, 1839.
(41) Choi, J.; Yee, A. F.; Laine, R. M. *Macromolecules* **2003**, *36*, 5666.
(42) Laine, R. M.; Choi, J.; Lee, I. *Adv. Mater.* **2001**, *13*, 800.
(43) Stockmayer, W. H.; Baur, M. E. *J. Am. Chem. Soc.* **1964**, *86*, 3485.
(44) Adachi, K.; Kotaka, T. *Prog. Polym. Sci.* **1993**, *18*, 585.
(45) Watanabe, H. *Prog. Polym. Sci.* **1999**, *24*, 1253.
(46) Watanabe, H. *Macromol. Rapid Commun.* **2001**, *22*, 127.
(47) Mijovic, J.; Miura, N.; Monetta, T.; Duan, Y. *Polym. News* **2001**, *26*, 251.
(48) Mijovic, J.; Sun, M.; Han, Y. *Macromolecules* **2002**, *35*, 6417.
(49) Mijovic, J.; Han, Y.; Sun, M.; Pejanovic, S. *Macromolecules* **2003**, *36*, 4589.
(50) Marcolli, C.; Calzaferri, G. *Appl. Organomet. Chem.* **1999**, *13*, 213.
(51) Wallace, W. E.; Guttman, C. M.; Antonucci, J. M. *Polymer* **2000**, *41*, 2219.
(52) Silverstein, R. M.; Webster, F. X.; Kiemle, D. *Spectrometric Identification of Organic Compounds*; John Wiley & Sons: New York, 1996.
(53) Chen, Y.; Iroh, J. O. *Chem. Mater.* **1999**, *11*, 1222.
(54) Denq, B.; Hu, Y.; Chen, L.; Chiu, W.; Wu, T. *J. Appl. Polym. Sci.* **1999**, *74*, 229.
(55) Williams, G. Theory of dielectric properties. In *Dielectric Spectroscopy of Polymeric Materials*; Runt, J. P., Fitzgerald, J. J., Eds.; American Chemical Society: Washington, DC, 1998.
(56) Williams, G. Dielectric relaxation spectroscopy of amorphous polymer systems: the modern approaches. In *Keynote Lectures in Selected Topics of Polymer Science*; CSIC: Madrid, 1997; Chapter 1, p 1.
(57) Kremer, F.; Schonhals, A. *Broadband Dielectric Spectroscopy*; Springer-Verlag: Berlin, 2002.
(58) Havriliak, S., Jr.; Negami, S. *Polymer* **1967**, *8*, 161.
(59) Cole, R. H.; Cole, K. S. *J. Chem. Phys.* **1942**, *10*, 98.
(60) Bian, Y.; Pejanovic, S.; Kenny, J.; Mijovic, J. *Macromolecules* **2007**, *40*, 6239.
(61) Hao, N.; Bohning, M.; Goering, H.; Schonhals, A. *Macromolecules* **2007**, *40*, 2955.
(62) Fischer, E. W.; Zetsche, A. *Polym. Prepr.* **1992**, *33*, 78.
(63) Katana, G.; Fischer, E. W.; Hack, T.; Abetz, V.; Kremer, F. *Macromolecules* **1995**, *28*, 2714.
(64) Kamath, S.; Colby, R. H.; Kumar, S.; Karatasos, K.; Floudas, G.; Fytas, G.; Roovers, J. E. L. *J. Chem. Phys.* **1999**, *111*, 6121.
(65) Winter, H. H.; Mours, M. *Adv. Polym. Sci.* **1997**, *134*, 165.
(66) Flory, P. J. *Principles of Polymer Chemistry*; Cornell University Press: Ithaca, NY, 1953.
(67) Buchenau, U. *J. Non-Cryst. Sol.* **2007**, *353*, 3812.

MA801044V